INORGANIC CHEMISTRY
FRONTIERS

RESEARCH ARTICLE

View Article Online
View Journal | View Issue

Cite this: *Inorg. Chem. Front.*, 2024, **11**, 5034

A lead-free zero-dimensional hybrid antimony halide perovskite X-ray scintillator with exceptional emission efficiency and excellent stability as a highly sensitive fluorescent probe†

Yu-Yin Wang,[a] Guo-Hao Jia,[a] Meng-Rui Huo,[a] Ming-Tao Cheng,[a] Xiang-Yu Chen,[a] Ai-Rui Chang,[a] Jie Zhang,[a] Yun-Yun Li[b] and Guo-Ming Lin *[c,d]

Received 5th May 2024,
Accepted 25th June 2024

DOI: 10.1039/d4qi01114g

rsc.li/frontiers-inorganic

Lead-free zero-dimensional (0D) hybrid antimony halide perovskites have emerged as promising materials for various optoelectronic and sensing applications, owing to their adjustable structural properties and non-toxic nature. In this study, we explore the photophysical characteristics, structural robustness, and sensing capabilities of $[FPPP]_2SbCl_7$ (FPPP = protonated 1-(2-fluorophenyl)piperazine). Employing a combination of experimental and theoretical approaches, we demonstrate its remarkable yellow light photoluminescence quantum yields (99.26%) and outstanding structural integrity. Moreover, investigations into the scintillation performance of $[FPPP]_2SbCl_7$ single crystals reveal high X-ray light yields (46 927 photons per MeV), a low detection limit (0.71 $\mu Gy_{air}\ s^{-1}$) and high-quality X-ray imaging, making them promising candidates for X-ray detection applications. Furthermore, $[FPPP]_2SbCl_7$ displays reversible fluorescence switching in response to nitrobenzene, showcasing its potential as a sensing platform for organic pollutants with outstanding repeatability and selectivity. Our findings not only deepen our comprehension of 0D hybrid antimony halides but also lay the groundwork for their utilization in diverse optoelectronic and sensing devices, opening new avenues for research in luminescent materials and detection applications.

Introduction

The detection and characterization of radiation are fundamental across numerous scientific and technological domains, with X-ray imaging standing out as indispensable in applications ranging from radiotherapy to noninvasive assessments and diverse scientific research.[1–6] Traditional rare earth-based inorganic scintillators have been the cornerstone of X-ray imaging due to their reliability and efficacy.[7] However, recent research has uncovered the promising potential of organometallic halide perovskites in this field. These materials demonstrate robust radioluminescence (RL) properties and efficient X-ray conversion, making them compelling candidates for next-generation scintillator materials.[8–11] Despite their potential, the development of stable scintillators remains challenging. Meanwhile, lead-based organometallic perovskite materials, commonly used in this context, face issues related to toxicity and vulnerability. In response to these challenges, researchers are increasingly investigating alternative materials that offer superior performance while addressing existing limitations. Among these alternatives, 0D hybrid antimony halide perovskites have emerged as particularly promising candidates.[12–15] These materials present significant advantages over lead-based materials, including non-toxicity and remarkable stability.[16–22] Their customizable structural properties and tunable characteristics make them highly desirable for a range of optoelectronic applications, notably in X-ray imaging.

The 0D architecture of antimony halides is defined by core structures enveloped within organic shells, effectively shielding them from various non-covalent interactions, including electrostatic forces, hydrogen bonding, and van der Waals interactions. This configuration often facilitates the formation of self-trapped excitons (STEs), leading to efficient and

---

[a] School of Chemistry, Chemical Engineering and Materials, Jining University, Qufu, Shandong, 273155, P. R. China

[b] Department of Chemical Engineering, College of Environmental and Biological Engineering, Putian University, Putian 351100, China

[c] Fujian Institute of Research on the Structure of Matter, Chinese Academy of Sciences, Fuzhou, Fujian 350002, China

[d] Department of Physics, National University of Singapore, Singapore 117551, Singapore. E-mail: lingmdbs@nus.edu.sg

† Electronic supplementary information (ESI) available: Crystallographic data in CIF format, and the table of crystal data is given in Table S1. CCDC 2328997. For ESI and crystallographic data in CIF or other electronic format see DOI: **https://doi.org/10.1039/d4qi01114g**

extensive light emission due to intense electron–phonon (EP) interactions. Moreover, the presence of Sb^{3+} cations, with their stereochemically active $5s^2$ lone pair, offers the potential to achieve diverse metal halide geometries, including square pyramids, tetrahedra, and octahedra, enabling the design of tailored optical emitters. For instance, Mao *et al.* investigated a range of hybrid antimony halides, such as A_2SbCl_5 and $A_2Sb_2Cl_8$ (where A denotes five distinct organic cations), showcasing the emission of red light from square pyramidal phosphors like A_2SbCl_5, peaking at 600 nm, while tetrahedrally configured structures like $A_2Sb_2Cl_8$ exhibited no discernible light emission.[22] Recent advancements made by Xia *et al.* introduced three hybrid compounds of antimony halides featuring dimeric $[Sb_2Cl_8]^{2-}$ anions, emitting broadband near-infrared or infrared signals.[23] These studies demonstrated the critical role of intense EP interactions in confining carriers generated by light exposure in low-dimensional hybrid metal halides, leading to the emission of STEs at low excited state energies.

Ongoing endeavors to improve organic–inorganic hybrid metal halide materials for X-ray scintillation focus on boosting the photoluminescence quantum yield (PLQY), lowering toxicity, enhancing stability, and exploring their broader applications across various fields. By leveraging the inherent advantages of 0D hybrid antimony halides, our objective is to surmount existing challenges and drive progress in scintillator technology. This study introduces $[FPPP]_2SbCl_7$, a novel 0D structured antimony halide, which exhibits vibrant yellow luminescence upon UV excitation and boasts a PLQY of 99.26%. Detailed analysis reveals its impressive X-ray scintillation light yield, low detection threshold and high-quality X-ray imaging capabilities. Furthermore, $[FPPP]_2SbCl_7$ exhibits reversible fluorescence switching in response to nitrobenzene, an organic pollutant, demonstrating remarkable repeatability, a low detection limit, and selectivity *via* fluorescence emission.

Experimental procedure

The details of reagents, experimental procedures, crystal synthesis processes and characterization methods are provided in the ESI.†

Results and discussion

Composition and structure

Bulk single crystals of $[FPPP]_2SbCl_7$ were synthesized using a low-temperature solvothermal reaction method as outlined in the Experimental section provided in the ESI.† X-ray diffraction analysis revealed the formation of a monoclinic phase of $[FPPP]_2SbCl_7$ with the *C*2/*c* space group. The structural arrangement consisted of discrete $[SbCl_6]^{3-}$ octahedra encircled by $[FPPP]^{2+}$ cations (Fig. 1a). These $[SbCl_6]^{3-}$ octahedra were effectively shielded by the $[FPPP]^{2+}$ cations (Fig. 1b), resulting in a 0D hydrogen bonding configuration at the molecular level. Furthermore, the $[FPPP]^{2+}$ cations formed a protective 2D layer around the discrete $[SbCl_6]^{3-}$ octahedra, further enhancing the structural stability. Each Sb^{3+} ion within the $[SbCl_6]^{3-}$ octahedron was coordinated with six Cl^- ions, with Sb–Cl bond distances ranging from 2.5178(3) to 2.7913(3) Å (Fig. 1c). The purity and crystallinity of $[FPPP]_2SbCl_7$ were validated through remarkable correspondence observed between actual and simulated powder X-ray diffraction (PXRD) data (Fig. S1†). The nearly identical diffraction peaks confirmed the high degree of crystallization achieved in the synthesized microcrystals. Moreover, individual chemical compositions were analyzed using energy-dispersive X-ray spectroscopy (EDS), as depicted through elemental mapping images and spectra, respectively (Fig. 1d and S2†). Subsequently, typical optical characterization techniques were employed to further explore the photophysical properties of the 0D antimony hybrid halides.

Photoluminescence properties of $[FPPP]_2SbCl_7$

The optically transparent bulk crystals of $[FPPP]_2SbCl_7$ displayed a vibrant yellow emission when excited with UV light. Moreover, these crystals exhibited distinct absorption edges with cut-off wavelengths at 423 nm (Fig. S3†). The PL properties of the synthesized crystals were investigated using steady-state and time-resolved PL spectra. Under excitation of a 358 nm UV source, the $[FPPP]_2SbCl_7$ crystals emitted broadband light centered around a wavelength of 556 nm, accompanied by a significant Stokes shift of 193 nm and a full width at half-maximum (FWHM) of 127 nm (Fig. 2a and S4†). The resulting commission internationale de l'éclairage (CIE) coordinates of (0.388, 0.512) positioned the crystals within the yellow region of the CIE chromaticity diagram (Fig. 2b). A series of three-dimensional PL excitation and emission maps obtained for the $[FPPP]_2SbCl_7$ samples identified a single emission center, indicating that the wide-ranging emissions originated from the relaxation of a common excited state (Fig. 2c). Furthermore, time-resolved PL spectra were acquired to delve into the emission mechanism. The average PL decay lifetime of $[FPPP]_2SbCl_7$ crystals at 300 K was determined to be 3.527 μs *via* double exponential fitting, exhibiting an increase to 4.042 μs at 80 K due to the increased radiative rate (Fig. 2d). Moreover, the negligible disparity observed in the PL emission spectra between microscale particles and bulk crystals dismissed the possibility of surface defects affecting light emission (Fig. S5†). In addition to their highly efficient broadband light emission, the $[FPPP]_2SbCl_7$ crystals demonstrated excellent spectral and structural stability. Thermogravimetric analysis revealed that the bulk crystals of $[FPPP]_2SbCl_7$ remained stable up to 280 °C (Fig. S6†). Furthermore, the prepared $[FPPP]_2SbCl_7$ crystals maintained a high degree of crystallinity and almost identical emission intensity even after prolonged exposure to a humid environment for about a month (Fig. S7 and S8†). Similar results were obtained after exposure to a strong xenon light source for 48 hours (Fig. S9 and S10†).

The broad FWHM, prolonged lifetime, and significant Stokes shift suggested that these broad-spectrum emissions stemmed from the radiative recombination of STEs, a phenom-

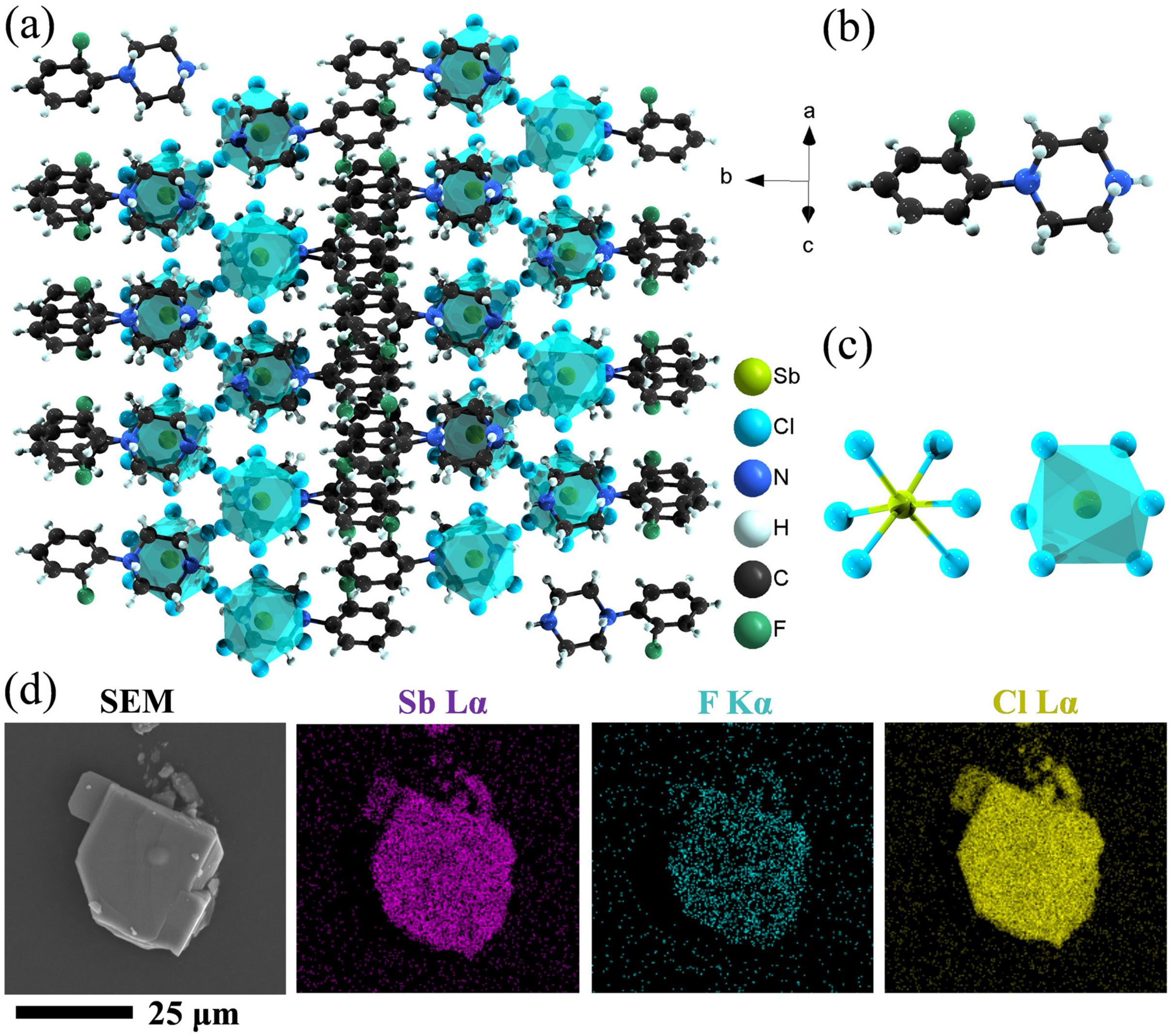

Fig. 1 The structural characterization of $[FPPP]_2SbCl_7$. (a) The arrangement of molecules in the prepared 0D sample as viewed towards the [101] plane. Structural diagrams of the $[FPPP]^{2+}$ cation (b) and the $[SbCl_6]^{3-}$ octahedron (c). (d) SEM images and the corresponding mapping of elements of the prepared microparticles, respectively.

enon previously observed in numerous 0D hybrid metal halide structures.[24] This assertion was bolstered by the observed linear correlation between excitation power density and emission intensity (Fig. 2e and f). The intense light emissions of the $[FPPP]_2SbCl_7$ crystals were substantiated by their remarkably high PLQY values, reaching 99.26% (Fig. 2g). Moreover, to delve deeper into the working principle of the PL effect and confirm the behavior of STEs, temperature-dependent PL emission spectroscopy was carried out across the same temperature range (Fig. 2h). The weak dependence of the emission wavelength on temperature may be attributed to relatively minor changes in the bandgap or thermal expansion effects that only marginally affect the emission properties. Additionally, the emission intensity exhibited a consistent increase as the temperature decreased from 300 K to 80 K, suggesting a reduction in the thermal quenching process and the non-radiative recombination rate. The thermal activation energy (E_a) was determined by fitting the integrated emission intensity with temperature using the Arrhenius equation:

$$I_{PL} = \frac{I_0}{1 + A\exp\left(-\frac{E_a}{k_B T}\right)}$$

Here, I_{PL} represents the integrated emission intensity at temperature T, I_0 denotes the integrated emission intensity at 0 K, k_B stands for the Boltzmann constant, and E_a signifies the exciton binding energy. The calculated value of E_a was found to be 266.7 meV, surpassing the thermal dissociation energy value of approximately 26 meV for free excitons at 300 K (Fig. 2i). This observation suggests the generation of stable bound excitons within the crystals of $[FPPP]_2SbCl_7$. Concurrently, the increase in temperature resulted in a gradual broadening of the emission spectra due to the enhancement in the EP coupling effect. Consequently, the high PLQY of

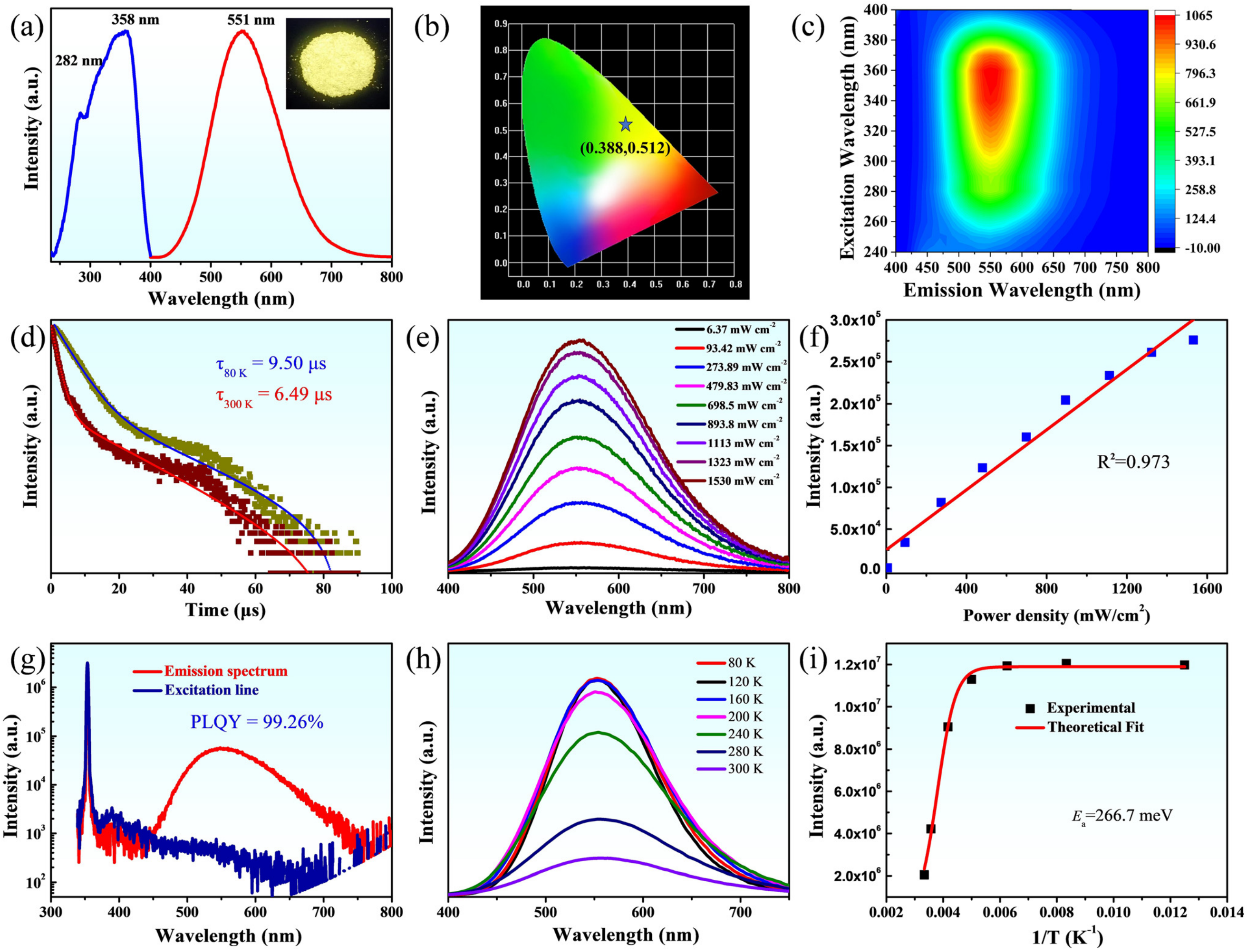

Fig. 2 The results acquired from the PL characterization of $[FPPP]_2SbCl_7$. (a) Excitation and emission spectra; inset: photo image of crystals under UV lamp irradiation (365 nm). (b) CIE chromaticity coordinates. (c) A 3D color map displaying the PL emission at varying temperatures. (d) Temperature-dependent PL decay curves at 80 K and 300 K. (e) Excitation power-dependent PL emission intensity of the compound. (f) A linear relationship exists between the excitation power density and the intensity of PL. (g) The PLQY of bulk crystals for the compound. (h) Temperature-dependent emission spectra of the compound. (i) Integrated PL intensity as a function of the reciprocal temperature.

$[FPPP]_2SbCl_7$ is primarily due to the unique zero-dimensional structure of the hybrid antimony halide perovskite. This structure leads to strong quantum confinement effects and reduces non-radiative recombination pathways, thus enhancing the PL efficiency.

Radioluminescence properties of $[FPPP]_2SbCl_7$

The scintillation performance of the synthesized $[FPPP]_2SbCl_7$ single crystals was comprehensively evaluated by examining parameters such as steady-state scintillation yield, scintillation decay time, afterglow under X-ray irradiation and detection limit. The optically transparent bulk crystals of $[FPPP]_2SbCl_7$ displayed a yellow emission under X-ray light (Fig. S11†). The steady-state scintillation light yield of $[FPPP]_2SbCl_7$ crystals was determined by comparing the integral intensity of their relative light with that of a LuAG : Ce reference (25 000 photons per MeV), ensuring an equal thickness of 3 mm and surface area for both samples. The light yield for the $[FPPP]_2SbCl_7$ sample was calculated using the formula 25 000 × (sample RL integral area/LuAG : Ce RL integral area), resulting in a scintillation yield of 46 927 photons per MeV for $[FPPP]_2SbCl_7$ (Fig. 3a). The emission peaks in RL for both crystals closely matched the PL emissions, suggesting minimal involvement of defect luminescence in the scintillation emission mechanism. Furthermore, the RL intensity increases with the dose rate ranging from ~5000 to ~50 000 $\mu Gy_{air}\ s^{-1}$ (Fig. 3b). Remarkably, the RL emission intensity exhibited a swift and consistent response to X-ray excitation, sustaining negligible attenuation even after 11 cycles (Fig. 3c). The dose rate of X-ray radiation was calibrated using an ion chamber dosimeter. Detection limits were determined through a series of calculations, comparing acquired X-ray excitation spectra under dark conditions with radiation doses maintained at specific, uniform column values. The detection limit was identified at

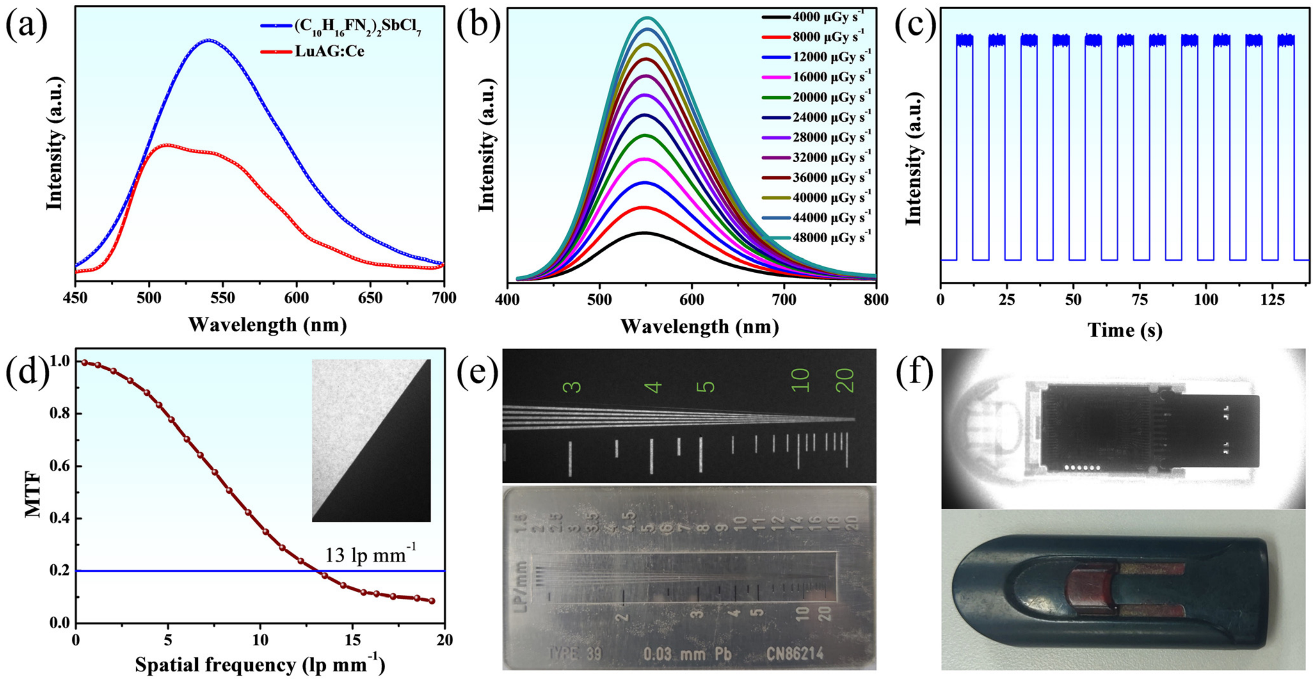

Fig. 3 (a) The RL spectra of $[FPPP]_2SbCl_7$ and LuAG : Ce under X-ray excitation; (b) the relationship between the RL intensity and dosage rate; (c) the intensity of RL as measured under cyclical X-ray irradiation; (d) curves of the modulation transfer function for $[FPPP]_2SbCl_7$ and a spatial resolution image; (e) bright field (bottom) and X-ray images (up) of the standard X-ray resolution test pattern plate obtained using the $[FPPP]_2SbCl_7$ scintillator; (f) sample as a scintillator under sunlight (bottom) and under X-ray irradiation (up).

an SNR value of 3 and calculated to be 0.71 $\mu Gy_{air}\ s^{-1}$ for $[FPPP]_2SbCl_7$. Notably, this detection limit is only 1/8 of the threshold required for X-ray medical diagnostics (5.5 $\mu Gy_{air}\ s^{-1}$). Spatial resolution assessment of the $[FPPP]_2SbCl_7$ screen reveals 13.01 lp mm^{-1} at a modulation transfer function (MTF) of 0.2 (Fig. 3d), comparable to the spatial resolutions of other metal halide-based scintillators. X-ray imaging employing a standard X-ray resolution test pattern plate surpassed 10 lp mm^{-1} observation limits (Fig. 3e). Strategically positioning a flash drive within the X-ray imaging platform and employing microscale $[FPPP]_2SbCl_7$ as a thin scintillation screen on transparent glass enable a comprehensive demonstration of its high-quality X-ray imaging capability (Fig. 3f), confirming its potential for future applications in radiography.

Insight into the photophysical mechanism of $[FPPP]_2SbCl_7$ single crystals

Subsequently, the Perdew–Burke–Ernzerhof (PBE) method was employed to conduct density functional theory (DFT) calculations, providing further insight into the photophysical characteristics of the 0D antimony hybrid halides. Analysis of the obtained band structure revealed nearly flat conduction bands (CBs) and valence bands (VBs) (Fig. 4a). This suggests minimal electronic coupling and highly confined electronic states. Consequently, the results indicate a significant quantum confinement effect with limited electronic interaction among neighboring inorganic anion clusters. These findings align well with previous observations of substantial distances between neighboring inorganic units. DFT calculations for the 0D antimony hybrid halide structure yielded a band gap value of 2.68 eV, which was underestimated compared to the experimentally measured value of 2.97 eV. This discrepancy may be attributed to the well-known declination associated with PBE-based band gap calculations. The density of states (DOS) analysis of the 0D antimony hybrid halide structure revealed that its valence band maximum (VBM) primarily consisted of Sb-4d and Cl-3p orbitals, while its conduction band minimum (CBM) included Sb-4d and Cl-3p orbitals along with contributions from the organic unit (Fig. 4b). The contour plots of partial charge density for the VBM and CBM in the 0D antimony hybrid halide structure are presented in Fig. 4c and d. The PL mechanism, as provided by the results of DFT calculations, indicated that both the valence and conduction bands were relatively flat, suggesting minimal electronic coupling among neighboring anionic octahedra. This implies that the formation of electron and hole polarons was facilitated by highly confined electron states with substantial effective masses. The organic cation and Sb are observed to contribute to the frontier orbitals, indicating that the PL properties of $[FPPP]_2SbCl_7$ depend on electronic transitions within both the cation and the anionic $[SbCl_6]^{4-}$ unit (Fig. 4e and f).

Small molecular fluorescence probe properties of $[FPPP]_2SbCl_7$

The distinctive and versatile properties of the 0D crystal structure of this halide framework were extensively explored to

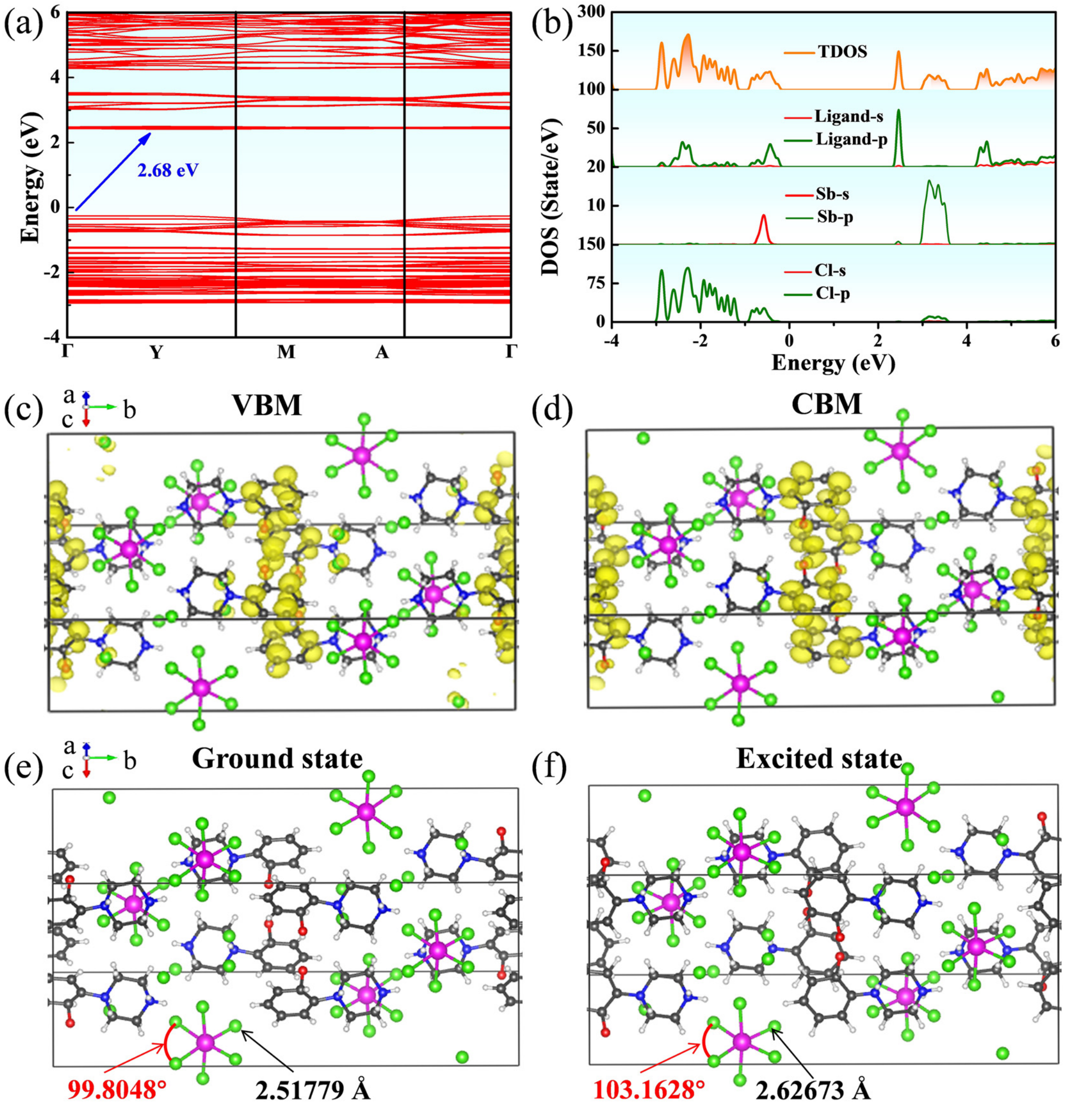

Fig. 4 The theoretical calculation of $[FPPP]_2SbCl_7$: (a) calculated electronic band structure and (b) the density of states (DOS) and partial DOS plots; (c) the valence band maximum and (d) the conduction band minimum; (e) the calculated excited state and (f) ground state.

uncover its potential for fluorescence switching triggered by small chemical molecules, serving as efficient fluorescent probes. PL emission was monitored before and after the addition of various organic solvents to the microcrystals to assess the sensing capability of $[FPPP]_2SbCl_7$ microcrystals. 4 mL of aromatic hydrocarbon derivatives, including methylbenzene ($C_6H_5CH_3$), iodobenzene (C_6H_5I), bromobenzene (C_6H_5Br), chlorobenzene (C_6H_5Cl), benzene (C_6H_6), ethylbenzene ($C_6H_5C_2H_5$) and nitrobenzene ($C_6H_5NO_2$), was utilized as the sensing target, respectively. PL emission spectroscopy revealed a drastic reduction in emission intensity to 0.72% due to the quenching effect of $C_6H_5NO_2$, while exhibiting no significant change with other solvents (Fig. 5a and b). Moreover, a variety of organic solvents with diverse functional groups were employed as external chemical perturbations to evaluate the PL quenching response to these stimuli. These solvents encompassed cyclohexane, tetrahydrofuran, acetonitrile and various alcohols. It was observed that the spectral profiles and intensities remained virtually unchanged from the initial data acquired for the freshly prepared sample even after the injection of these organic solvents for over 24 hours, indicating no fluorescence quenching in these cases (Fig. S12†). The detection limit, as a crucial parameter indicative of sensing ability, was evaluated through fluorescence titration experiments using a series of diluted $C_6H_5NO_2$/toluene solutions with concentrations ranging from 10 ppm to 1000 ppm. Optical images and PL spectra (Fig. 5c and d) revealed significant fluorescence quenching until the concentration of the $C_6H_5NO_2$/toluene solution was reduced to 50 ppm. Crucially, the diminished fluorescence of the $[FPPP]_2SbCl_7$ microcrystals induced by $C_6H_5NO_2$ could be fully restored upon rinsing them with toluene, with the recovered

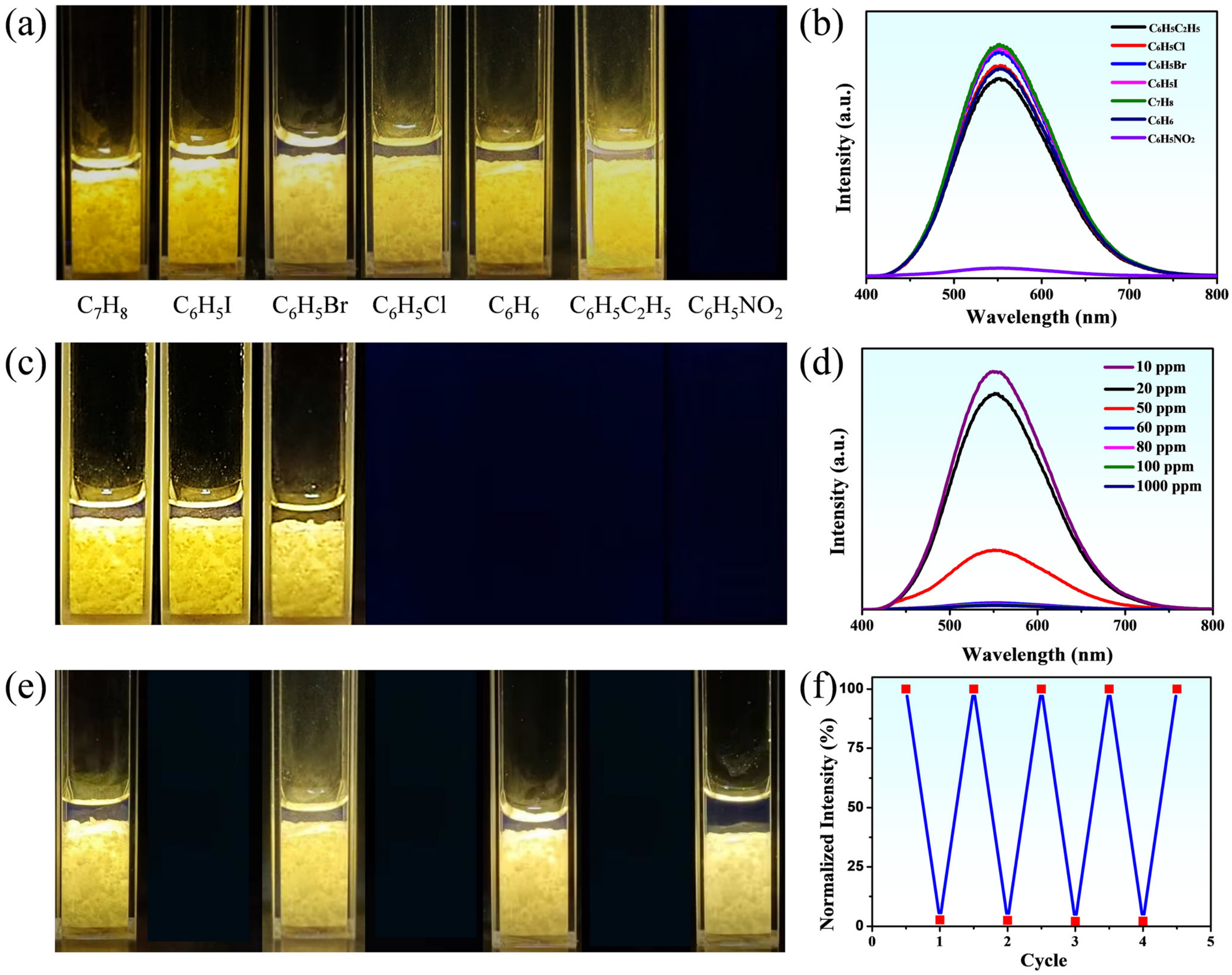

Fig. 5 The results of fluorescent probe characterization of the $[FPPP]_2SbCl_7$ microcrystals. (a) Optical images and (b) PL emission spectra after the addition of different types of organic solvents. (c) Optical images and (d) PL emission spectra following the addition of $C_6H_5NO_2$ at varying concentrations by volume. (e) Optical images and (f) PL intensity of the microcrystals depicting a consistent cycle of quenching and recovery with minimal reduction in their emission intensity after 4 cycles.

fluorescence intensity nearly matching the initial value. This compellingly demonstrated the reversible PL switching ability of $[FPPP]_2SbCl_7$ towards $C_6H_5NO_2$. To confirm the consistency of this reversible quenching–recovery process, the change in the PL emission intensity of the $[FPPP]_2SbCl_7$ microcrystals was monitored over impregnation-washing cycles. The optical images of the microcrystals depicted a consistent cycle of quenching and recovery, with minimal reduction in their emission intensity after 4 cycles, demonstrating exceptional repeatability and reversibility (Fig. 5e and f). The reversible fluorescence quenching observed in $[FPPP]_2SbCl_7$ upon exposure to $C_6H_5NO_2$ is ascribed to charge transfer from $[SbCl_6]^{3-}$ to electron-deficient nitrobenzene molecules adsorbed on the surface of $[FPPP]_2SbCl_7$.[25] These findings underscore the potential of $[FPPP]_2SbCl_7$ microcrystals as effective fluorescent probes for detecting $C_6H_5NO_2$ with high repeatability, selectivity, and sensitivity. This marks the development of a novel antimony halide-based fluorescent probe for detecting $C_6H_5NO_2$, thereby advancing detection applications employing luminescent materials based on metal halides.

Conclusion

In conclusion, this study investigates the remarkable potential of lead-free 0D hybrid antimony halides, specifically $[FPPP]_2SbCl_7$, as scintillators and fluorescent probes. The synthesized $[FPPP]_2SbCl_7$ crystals exhibited an exceptional PLQY of 99.26% and high structural stability. The scintillation performance of $[FPPP]_2SbCl_7$ single crystals displayed high X-ray light yields, a low detection limit and rapid decay times, making them suitable for X-ray detection imaging. Furthermore, the high sensitivity and reversible fluorescence switching ability of $[FPPP]_2SbCl_7$ towards nitrobenzene underscore its potential as a sensing platform for organic pollutant detection. Overall, our comprehensive investigation into its photophysical properties, structural integrity, and sensing capabilities has highlighted its efficacy across a wide range of applications.

Data availability

The data supporting this article have been included as part of the ESI.†

Crystallographic data for $(C_{10}H_{16}FN_2)_2SbCl_7$ have been deposited at the CCDC under 2328997 and can be obtained from the CCDC *via* their website **https://www.ccdc.cam.ac.uk**.

Conflicts of interest

The authors declare no conflict of interest.

Acknowledgements

We acknowledge the financial support from the National Natural Science Foundation of China (No. 22201099 and 22101282), the Shandong Provincial Natural Science Foundation (ZR2021QB204), and the Jining University 2019, 2020 "100 Outstanding Talents" support program cultivation project (2020ZYRC02). This work is also supported by the University Feature Laboratory for Energy Conversion and Nanocatalysis of Shandong Province.

References

1 Y. C. Kim, H. K. Kwang, D.-Y. Son, D.-N. Jeong, J.-Y. Seo, Y. S. Choi, I. T. Han, S. Y. Lee and N. G. Parket, Printable organometallic perovskite enables large-area, low-dose X-ray imaging, *Nature*, 2017, **550**, 87–91.

2 Y. Li, W. Shao, X. Ouyang, Z. Zhu, H. Zhang, X. Ouyang, B. Liu and Q. Xu, Scintillation properties of perovskite single crystals, *J. Phys. Chem. C*, 2019, **123**, 17449–17453.

3 X. Mei, H.-C. Lee, K.-Y. Diao, M. Huang, B. Lin, C. Liu, Z. Xie, Y. Ma, P. M. Robson, M. Chung, A. Bernheim, V. Mani, C. Calcagno, K. Li, S. Li, H. Shan, J. Lv, T. Zhao, J. Xia, Q. Long, S. Steinberger, A. Jacobi, T. Deyer, M. Luksza, F. Liu, B. P. Little, Z. A. Fayad and Y. Yang, Artificial intelligence–enabled rapid diagnosis of patients with COVID-19, *Nat. Med.*, 2020, **26**, 1224–1228.

4 M. J. Weber, Inorganic scintillators: today and tomorrow, *J. Lumin.*, 2002, **100**, 35–45.

5 S. M. Lee, J. B. Seo, J. Yun, Y.-H. Cho, J. Vogel-Claussen, M. L. Schiebler, W. B. Gefter, E. J. R. van Beek, J. M. Goo, K. S. Lee, H. Hatabu, J. Gee and N. Kim, Deep learning applications in chest radiography and computed tomography current state of the art, *J. Thorac. Imaging*, 2019, **34**, 75–85.

6 O. Rabin, J. M. Perez, J. Grimm, G. Wojtkiewicz and R. Weissleder, An X-ray computed tomography imaging agent based on long-circulating bismuth sulphide nanoparticles, *Nat. Mater.*, 2006, **5**, 118–122.

7 H. S. Lee, H. C. Bhang, J. H. Choi, H. Dao, I. S. Hahn, M. J. Hwang, S. W. Jung, W. G. Kang, D. W. Kim, H. J. Kim, S. C. Kim, S. K. Kim, Y. D. Kim, J. W. Kwak, Y. J. Kwon, J. Lee, J. H. Lee, J. I. Lee, M. J. Lee, S. J. Lee, J. Li, X. Li, Y. J. Li, S. S. Myung, S. Ryu, J. H. So, Q. Yue and J. J. Zhu, Limits on interactions between weakly interacting massive particles and nucleons obtained with CsI(Tl) crystal detectors, *Phys. Rev. Lett.*, 2007, **99**, 091301.

8 K. Okazaki, H. Fukushima, D. Nakauchi, G. Okada, D. Onoda, T. Kato, N. Kawaguchi and T. Yanagida, Investigation of $Er : Bi_4Ge_3O_{12}$ single crystals emitting near-infrared luminescence for scintillation detectors, *J. Alloys Compd.*, 2022, **903**, 163834.

9 A. M. Priya, R. K. Selvan, B. Senthilkumar, M. K. Satheeshkumar and C. Sanjeeviraja, Synthesis and characterization of $CdWO_4$ nanocrystals, *Ceram. Int.*, 2011, **37**, 2485–2488.

10 H. Makii, S. Ota, T. Ishii, K. Nishio, I. Nishinaka, K. Furutaka, Y. Wakabayashi, S. Chiba and M. Igashira, Development of anti-compton $LaBr_3$(Ce) spectrometer for measurement of surrogate reactions, *Nucl. Data Sheets*, 2014, **119**, 361–364.

11 A. C. Wibowo, C. D. Malliakas, Z. Liu, J. A. Peters, M. Sebastian, D. Young Chung, B. W. Wessels and M. G. Kanatzidis, Photoconductivity in the chalcohalide semiconductor, SbSeI: a new candidate for hard radiation detection, *Inorg. Chem.*, 2013, **52**, 7045–7050.

12 Z. Xing, Z. Zhou, G. Zhong, C. C. S. Chan, Y. Li, X. Zou, J. E. Halpert, H. Su and K. S. Wong, Barrierless exciton self-trapping and emission mechanism in low-dimensional copper halides, *Adv. Funct. Mater.*, 2022, **32**, 2207638.

13 F. Jiang, Z. Wu, M. Lu, Y. Gao, X. Li, X. Bai, Y. Ji and Y. Zhang, Broadband emission origin in metal halide perovskites: are self-trapped excitons or ions?, *Adv. Mater.*, 2023, **35**, 2211088.

14 S. Zhou, Y. Chen, K. Li, X. Liu, T. Zhang, W. Shen, M. Li, L. Zhou and R. He, Photophysical studies for Cu(i)-based halides: broad excitation bands and highly efficient single-component warm white-light-emitting diodes, *Chem. Sci.*, 2023, **14**, 5415–5424.

15 G. Xu, C. Wang, Y. Li, W. Meng, G. Luo, M. Peng, B. Xu and Z. Deng, Solid-state synthesis of cesium manganese halide nanocrystals in glass with bright and broad red emission for white LEDs, *Chem. Sci.*, 2023, **14**, 5309–5315.

16 Q. He, C. Zhou, L. Xu, S. J. Lee, X. Lin, J. Zeu, M. Worku, M. Chaaban and B. Ma, Highly stable organic antimony halide crystals for X-ray scintillation, *ACS Mater. Lett.*, 2020, **2**, 633–638.

17 B. Zhou, Z. Qi, M. Dai, C. Xing and D. Yan, Ultralow-loss optical waveguides through balancing deep-blue TADF and orange room temperature phosphorescence in hybrid antimony halide microstructures, *Angew. Chem., Int. Ed.*, 2023, **62**, e202309913.

18 B. Li, J. Jin, M. Yin, X. Zhang, M. S. Molokeev, Z. Xia and Y. Xu, Sequential and reversible phase transformations in zero-dimensional organic-inorganic hybrid Sb-based halides towards multiple emissions, *Angew. Chem., Int. Ed.*, 2022, **61**, e202212741.

19 Y. Wu, C.-M. Shi, L.-J. Xu, M. Yang and Z.-N. Chen, Reversible luminescent vapochromism of a zero-dimensional Sb^{3+}-doped organic–inorganic hybrid, *J. Phys. Chem. Lett.*, 2021, **12**, 3288–3294.

20 K. M. McCall, V. Morad, B. M. Benin and M. V. Kovalenko, Efficient lone-pair-driven luminescence: structure–property relationships in emissive $5s^2$ metal halides, *ACS Mater. Lett.*, 2020, **2**, 1218–1232.

21 Z. Zhang, Y. Lin, J. Jin, L. Gong, Y. Peng, Y. Song, N. Shen, Z. Wang, K. Du and X. Huang, Crystalline-phase-recognition-induced domino phase transition and luminescence switching for advanced information encryption, *Angew. Chem., Int. Ed.*, 2021, **60**, 23373–23379.

22 C. Sun, Z. Deng, Z. Li, Z. Chen, X. Zhang, J. Chen, H. Lu, P. Canepa, R. Chen and L. Mao, Achieving near-unity photoluminescence quantum yields in organic-inorganic hybrid antimony(III) chlorides with the $[SbCl_5]$ geometry, *Angew. Chem., Int. Ed.*, 2023, **62**, e202216720.

23 B. Su, S. Geng, Z. Xiao and Z. Xia, Highly distorted antimony(III) chloride $[Sb_2Cl_8]^{2-}$ dimers for near-infrared luminescence up to 1070 nm, *Angew. Chem., Int. Ed.*, 2022, **61**, e202208881.

24 Z. Li, Y. Li, P. Liang, T. Zhou, L. Wang and R.-J. Xie, Dual-band luminescent lead-free antimony chloride halides with near-unity photoluminescence quantum efficiency, *Chem. Mater.*, 2019, **31**, 9363–9371.

25 Y.-B. Lu, Y.-Q. Liao, L. Dong, S.-D. Zhu, H.-R. Wen, J. Huang, X.-X. Dai, P. Lian, X.-M. Jiang, R. Li and Y.-R. Xie, Ultra-stable metal–organic framework with concurrent high proton conductivity and fluorescence sensing for nitrobenzene, *Chem. Mater.*, 2021, **33**, 7858–7868.